Accepted Manuscript

Towards stochastic discrete element modelling of spherical particles with surface roughness: A normal interaction law

Y.T. Feng, T. Zhao, J. Kato, W. Zhou

PII: S0045-7825(16)30928-8
DOI: http://dx.doi.org/10.1016/j.cma.2016.10.031
Reference: CMA 11192

To appear in: *Comput. Methods Appl. Mech. Engrg.*

Received date: 15 August 2016
Revised date: 17 October 2016
Accepted date: 24 October 2016

Please cite this article as: Y.T. Feng, T. Zhao, J. Kato, W. Zhou, Towards stochastic discrete element modelling of spherical particles with surface roughness: A normal interaction law, *Comput. Methods Appl. Mech. Engrg.* (2016), http://dx.doi.org/10.1016/j.cma.2016.10.031

Towards Stochastic Discrete Element Modelling of Spherical Particles with Surface Roughness: A Normal Interaction Law

Y. T. Feng[1,2]*, T. Zhao[1], J. Kato[1], and W. Zhou[2]
[1]Zienkiewicz Centre for Computational Engineering, Swansea University, UK
[2]State Key Laboratory of Water Resources and Hydropower Engineering Science
Wuhan University, Wuhan, China 430072

Abstract

The current work is the first attempt towards establishing a stochastic discrete element modelling framework by developing a normal contact interaction law based on the classic Greenwood and Williamson (GW) model for spheres with rough surfaces. Two non-dimensional forms of the model that have a substantial impact on the computational efficiency are discussed and the theoretical relationship between the GW model and the Hertzian model for smooth spheres is formally established. Due to the inter-dependence between the contact pressure and deformation distributions in the model, a Newton-Raphson based iterative solution procedure is proposed to effectively and accurately obtain the contact force in terms of the overlap and two surface roughness parameters. The related key components of the procedure are addressed in detail. The numerical results obtained are first validated and then curve-fitted to derive an empirical formula as a new normal interaction law for spheres with surface roughness. The explicit nature of the new interaction law makes it readily be incorporated into the current discrete element modelling framework. A simple example is presented to illustrate the effect of surface roughness on the packing behaviour of a particle assembly.

KEYWORDS: Stochastic discrete element modelling, Greenwood and Williamson model, Surface roughness; Normal contact law

1 Introduction

The discrete element method (DEM) [1] has emerged over the last two decades as a powerful computational technique to simulate and predicte the behavior of systems of a particulate or discrete nature in many scientific and engineering applications [5]. The basic procedure of the DEM involves: 1) to represent particles as rigid geometric entities in various packing configurations; 2) to conduct contact detection to evaluate interaction forces between particles based on some appropriate physically based interaction laws; and 3) to assemble all the forces acting on each particle and to numerically solve the resulting dynamic equations of particles in the system to update their accelerations, velocities and positions at discrete time instants. This computational framework of the DEM is essentially *deterministic* in that all the input parameters and loading conditions must be known *in prior*, and the system behaviour is determined in a definitive manner. However, a significant degree of randomness

*Corresponding author; e-mail: y.feng@swansea.ac.uk

and uncertainty exists in all practical problems, leading to stochastic processes in terms of particle motion; whereas a DEM solution for a given problem is, at most, one realisation in the context of Monte Carlo simulations. Therefore it is of both theoretical and practical importance that a stochastic discrete element modelling (SDEM) methodology be developed.

From the perspective of the geometric representation in the DEM, the most commonly used primitive geometric entities are disks and spheres, with ellipses and ellipsoids used to a much lesser extent, but all assumed to have smooth surfaces. However, real particles contain geometric irregularities or randomness at both microscopic and macroscopic levels. By recognising the significant influence of particle shapes on the mechanical behaviour of particle systems, the current discrete element modelling of irregularities of real particles has mostly been focused on the macroscopic level. In addition to the introduction of non-spherical entities such as polygons, polyhedra, super-quadrics, cylinders *etc.* [10, 11], more complicated geometric shapes are often represented by bonding or clumping together several basic entities [6, 7, 8, 9, 12]. Nevertheless, surface irregularities at the microscopic level, also called the surface roughness, are more difficult to be accounted for, although they may have strong influence on the phenomena of contact, friction, wear and lubrication [13].

The contact laws mostly employed in the DEM, such as the linear contact model and the Hertzian contact model, are intended for contact between smooth particles. It is therefore necessary to quantitatively improve the classical DEM by taking the surface roughness into consideration.

Several approaches have been developed to understand the contact mechanism between rough surfaces. Two key issues need to be addressed: the mathematical description of rough surfaces, and the modelling of microscopic contact mechanisms. The modelling of rough surfaces can be classified into two categories: *statistical* and *deterministic*. The earliest and most recognized statistical treatment of rough surfaces is the Greenwood and Williamson (GW) model [2], in which a rough surface is described as an assembly of asperities whose properties are obtained from a given statistical height distribution, and then the Hertzian contact solution is applied to each asperity to obtain an overall contact pressure distribution. For the contact between two rough curved bodies instead of two nominally flat surfaces, the first analytical investigation is conducted by Greenwood and Tripp [3] who employ the GW asperity contact model together with the bulk surface deformation for circular point contact.

The GW model can be viewed as a single scale method since the statistical parameters used to represent rough surfaces are scale-dependent. An early attempt of using multi-scale methods is made by Archard [14] who models the asperities of rough surface as *protuberance* upon *protuberance*. Another statistical approach is introduced by Majumdar and Bhushan [15], where a fractal curve/surface is adopted to describe a rough surface, together with a contact mechanism to resolve the contact. This fractal based approach can be regarded as multiple scaled because of the inherent multi-scale invariant characteristics of the most fractal curves/surfaces.

On the other hand, the deterministic methods attempt to model rough surfaces in a definitive manner and the resulting contact problem is typically solved by the finite element method. Furthermore, the fast Fourier transformation can also be used to represent rough surfaces [16].

Apart from the modelling of rough surfaces, most research work focus on microscopic contact mechanisms. For purely elastic contact, the Hertzian contact model is applied. More complicated material models, such as elasto-plastic contact models, are developed by Chang *et al.* [17], Zhao *et al.* [18], Jackson and Green [19], and others [21, 22, 23]. Beheshti and

Khonsari [24] employ different statistical micro-contact models, along with the elastic bulk deformation formula of the line contact [20], for an elliptical point contact to determine the impact of surface roughness on various contact characteristics. The maximum normal pressure, contact width and real contact area from different contact models are also compared, and some predictive formulas are proposed to predict these quantities.

However these formulas contain many parameters and coefficients, making them less favorable to be readily adopted in the DEM. In addition, the formulas are *force-driven* in the sense that the total contact force is supposed to be given. This is a common feature in most existing work on the GW model, and thus is not fully consistent with the DEM where the interaction laws are mainly *overlap-driven*.

As the first step towards developing a stochastic discrete element modelling framework, the main objective of this paper is to establish a new normal interaction law based on the GW model for spherical particles with random rough surfaces. The GW model is chosen as the basis due to its simplicity and popularity. The current work is a significant advancement of the initial work of Kato [25] and the most recent work of Feng *et al.* [26].

In the next section, a brief description of the GW model for flat surfaces and spheres with surface roughness is provided. Two non-dimensional forms of the model that have a substantial impact on reducing computational costs are discussed in Section 3. Section 4 establishes the theoretical relationship between the GW model and the Hertzian model for smooth spheres. Due to the implicit nature of the GW model, numerical solutions must be utilised to obtain the contact force when the overlap and the surface roughness parameters are given. An effective and accurate numerical solution procedure in the context of Newton-Raphson iterations is proposed in Section 5, and the related computational issues that are crucial to the effectiveness and accuracy of the numerical procedure are addressed in detail. Section 6 discusses the selection of some parameters included in the model and the numerical procedure, and the validation of the numerical results against some known results in the literature. Based on numerical simulations, Section 7 is devoted to the development of an explicit empirical formula as a new normal interaction law. Then an illustrative example is presented in Section 8 to demonstrate the effects of surface roughness on the packing behaviour of a particle system. Finally, concluding remarks are made in Section 9.

2 The Classic GW Model

A rough surface consists of a myriad of asperities or peaks that restrict the real contact area when two such surfaces are in contact. Due to the complexity of a rough surface, an appropriate mathematical expression is needed to model a real surface as a profile with a particular statistical distribution of asperities, for instance, the Gaussian or the exponential distribution. This statistical approach to mathematically represent rough surfaces is adopted in the GW model [2]. By further combining with the Hertzian elastic theory, a solution to the contact problem of rough surfaces is derived.

Several assumptions are made in the classic GW model: 1) The height profile of a rough surface is assumed to obey a Gaussian distribution; 2) The summits of the asperities are spherical with constant curvature; 3) Each individual asperity deforms separately; and 4) The bulk surface deformation below the individual asperity is negligible.

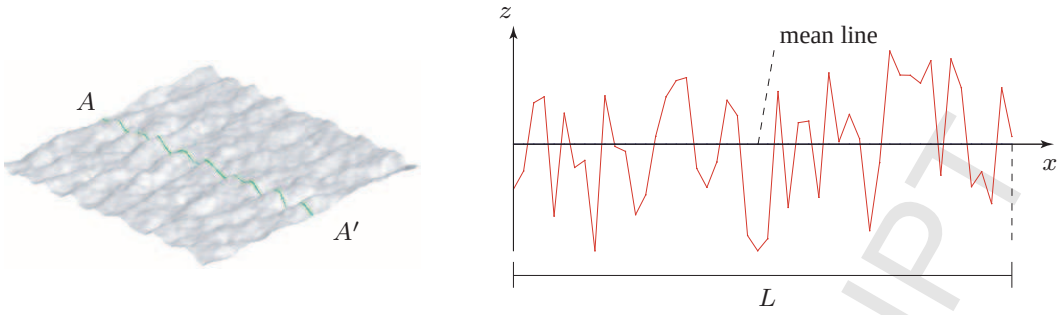

(a) 3D rough surface

(b) Profile of the cross section $A - A'$

Figure 1: Topography of a rough surface

2.1 Characteristics of rough surfaces

The characteristics of a rough surface are obtained on the basis of the profile which is the line of a cross section in a direction perpendicular to the surface as shown in Figure 1. From this profile, surface roughness parameters are determined by scrutinising a set of points $z(x_i)(i = 1, \cdots, N)$ which give the heights from the mean line in the sample length interval L. The main surface roughness parameters include:

1). Root mean square roughness σ: This parameter, also called RMS, is the standard deviation of the height distribution of a surface from its mean line

$$\sigma = \sqrt{\frac{1}{L}\int_0^L z^2(x)dx} \tag{1}$$

2). Probability density function ϕ: The probability density function, also known as the amplitude density in statistics, represents the distribution spectrum of a profile height and can be expressed by plotting the density of the profile height shown in Figure 2.

In order to obtain the probability density, the height of a profile is divided into layers with small increment dz. Comparing the length of the profile laying between z and $z+dz$ with the total length of the profile gives rise to the probability $P(z < Z < z+dz)$, thus the probability density can be written as

$$\phi(z) = \lim_{dz\to 0} \frac{P(z < Z < z + dz)}{dz} \tag{2}$$

In the GW model, it is assumed that the height distribution obeys the following Gaussian or normal probability density function

$$\mathcal{N}(0, \sigma^2): \quad \phi(z) = \frac{1}{\sqrt{2\pi\sigma^2}} \exp\big(-\frac{z^2}{2\sigma^2}\big) \tag{3}$$

2.2 Contact of two nominally flat rough surfaces

Consider the contact problem of two nominally flat rough surfaces which are assumed to have RMS roughness values σ_1 and σ_2 respectively, and have a separation distance d between their nominal surfaces. The problem can be further reduced to the contact of a rigid smooth flat surface with a deformable rough flat surface of an equivalent RMS roughness (due to the Gaussian distributions)

$$\sigma^2 = \sigma_1^2 + \sigma_2^2$$

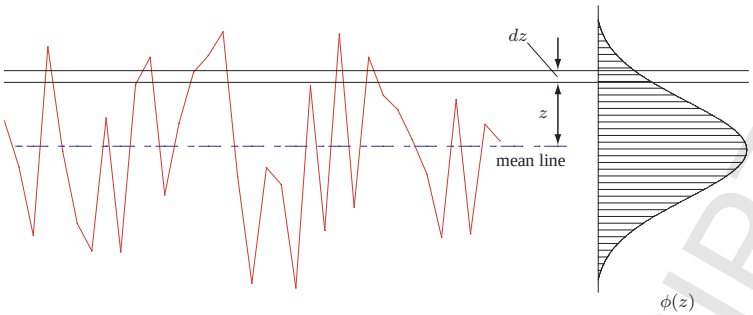

Figure 2: Profile heights and probability density of summits

The height profile of the rough surface is described by the summit height z, the mean summit line and the probability function $\phi(z)$ as shown in Figure 2.

As mentioned above, all the summits are assumed to have the same radius β and there are N summits in the nominal surface area. Since the overlap between the flat surface and an asperity with height z_s greater than the separation d is $z_s - d$, the contact force f of the summit of the asperity for a linear elastic contact is defined by the Hertzian theory as

$$f(z_s) = \frac{4}{3} E \beta^{1/2} (z_s - d)^{3/2} \tag{4}$$

where E is the equivalent Young's modulus of the two contacting surfaces.

The probability of having a contact at any given asperity of height z_s is

$$\text{prob}(z_s > d) = \int_d^\infty \phi(z_s)\, dz_s \tag{5}$$

Then the total contact force experienced by the nominal surface area, in terms of separation d, is

$$P(d) = N \int_d^\infty f(z_s)\phi(z_s)\, dz_s = \frac{4}{3} E N \beta^{1/2} \int_d^\infty (z_s - d)^{3/2} \phi(z_s)\, dz_s \tag{6}$$

2.3 Contact of two rough spheres

When the above GW theory is applied to the contact problem of two rough spheres, the only difference is in the geometric aspect. Under the assumption that the distribution of asperity heights is *stationary* as a random field, the contact problem between two rough spheres can still be treated as *axi-symmetric*. Because of the spherical profile, the separation between the two spheres will be a function of r, the distance from the centre of the contact area. The contact problem between two rough spheres can be made equivalent to the contact between a *deformable* smooth sphere of radius R and a nominally *rigid* flat rough surface having a Gaussian distribution of asperity heights with RMS σ. The equivalent R and σ can be obtained by the radii and roughness parameters of the two spheres using the following relationships:

$$\frac{1}{R} = \frac{1}{R_1} + \frac{1}{R_2}; \quad \sigma^2 = \sigma_{s_1}^2 + \sigma_{s_2}^2 \tag{7}$$

in which subscripts 1 and 2 indicate the surface numbers.

Referring to Figure 3, z_0 is the *separation* between the non-deformed configuration of the sphere and the mean line of the flat surface. To make it compatible with the convention of

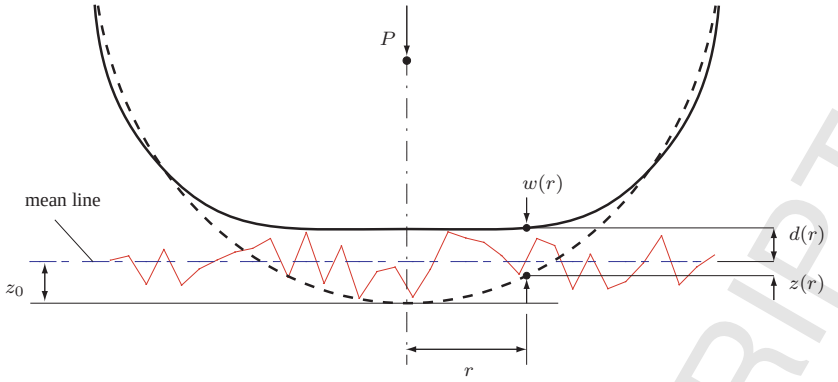

Figure 3: Contact between a smooth sphere and a nominally flat rough surface

the DEM, z_0 is assumed to be negative when the two surfaces are in separation, and positive in overlap. In what follows, z_0 is also set to be the *overlap* $\delta = z_0$. Thus, all the contact related quantities, such as pressure and deformation distributions and total force, will be explicit or implicit functions of the given δ.

When $\delta > 0$, the corresponding Hertzian solutions for the smooth spheres are given below for future reference:

$$\text{Contact radius:} \quad a = \sqrt{R\delta} \tag{8}$$

$$\text{Pressure distribution:} \quad p_h(r) = p_{h0}\left(1 - \frac{r^2}{a^2}\right)^{1/2}; \quad p_0 = \frac{2E}{\pi}\frac{a}{R}; \quad r \in [0, a] \tag{9}$$

$$\text{Deformation distribution:} \quad w_h(r) = w_{h0}\left(1 - \frac{r^2}{2a^2}\right) = z_0 - \frac{r^2}{2R}; \quad w_{h_0} = \delta; \quad r \in [0, a] \tag{10}$$

$$\text{Total force:} \quad P_h(\delta) = \frac{4}{3}Ea\delta = \frac{4}{3}E\sqrt{R}\delta^{3/2} \tag{11}$$

The profile of the un-deformed sphere can be described by

$$z(r) = z_0 - \frac{r^2}{2R} \tag{12}$$

Then the separation between the deformed sphere and the nominal flat surface at r is

$$d(r) = w(r) - z_0 + \frac{r^2}{2R} \tag{13}$$

where $w(r)$ is the (bulk) deformation of the sphere. The overlap of the asperity of height z_s at r with the sphere is

$$\delta(r) = z_s - d(r) \tag{14}$$

When $\delta(r) > 0$, the elastic contact force between the sphere and the asperity is defined by

$$f(z_s) = \frac{4}{3}E\beta^{1/2}[z_s - d(r)]^{3/2} \tag{15}$$

and the average pressure at r can be approximated by

$$p_s(r) = Nf(z_s) = c[z_s - d(r)]^{3/2}; \; c = \frac{4}{3}E\beta^{1/2}; \; z_s > d(r) \tag{16}$$

where N now is the asperity density, i.e. the number of asperities per unit area. By further considering the probability distribution of the summit heights, the effective, or expected contact pressure distribution over the entire contact area can be expressed as

$$p(r) = \int_{d(r)}^{+\infty} p_s(r)\phi(z_s)\,dz_s = C\int_{d(r)}^{+\infty}[z_s - d(r)]^{3/2}\phi(z_s)\,dz_s \tag{17}$$

where

$$C = \frac{4}{3}EN\beta^{1/2} \tag{18}$$

in which β denotes the radius of the asperities. Replacing $d(r)$ by (13) results in an alternative form

$$p(r) = C\int_{w(r)+\frac{r^2}{2R}}^{\infty}\left[z_s - w(r) - \frac{r^2}{2R}\right]^{3/2}\phi(z_s - \delta)\,dz_s \tag{19}$$

The deformation of the sphere $w(r)$ can be obtained from the solution to the axi-symmetric deformation of an elastic half-space subject to the pressure $p(r)$ as follows [4]

$$w(r) = \frac{4}{\pi E}\int_0^{\bar{a}}\frac{t}{r+t}p(t)\mathbf{K}(k)\,dt \tag{20}$$

where $\mathbf{K}(k)$ is the complete elliptic integral of first kind with the elliptic modulus (non-dimensional)

$$k = \frac{2\sqrt{rt}}{r+t}$$

and $\bar{a}$ is the radius of the contact area, which is larger than the Hertzian contact radius a.

By integrating the pressure distribution (17) or (19) over the contact radius $\bar{a}$, the total contact force P between the sphere and the rough flat surface with overlap δ can be obtained by

$$P(\delta) = \int_0^{\bar{a}} 2\pi r p(r)\,dr \tag{21}$$

3 The GW model: Non-Dimensional Forms

There are three parameters in Equation (17) or (19) that are associated with the surface roughness: N, β and σ, but only σ and $N\beta^{1/2}$ are independent. σ has a clear geometric meaning and can be reasonably defined for a given pair of surfaces (spheres). However this may not be the case for $N\beta^{1/2}$, and in particular, its value range can be very large.

A non-dimensional parameter, μ, is defined in [3] as

$$\mu = \frac{8}{3}\sigma N\sqrt{2R\beta} \tag{22}$$

Compared to $N\beta^{1/2}$, μ has a much narrower range, as stated in [4], therefore is adopted here to replace $N\beta^{1/2}$ as the second independent parameter. Since

$$N\beta^{1/2} = \frac{3\mu}{8\sqrt{2R}\sigma} \tag{23}$$

the coefficient C defined by (18) can be expressed in terms of σ and μ as

$$C = \frac{\mu}{\sqrt{8R\sigma}}E \tag{24}$$

Table 1: The scaling factors in two non-dimensional forms

q^*	σ-form	δ-form
δ^*	σ	-
σ^*	-	δ
w^*	σ	δ
z_s^*	σ	δ
$\phi^*(z_s^*)$	$1/\sigma$	$1/\delta$
r^*	$\sqrt{2R\sigma}$	$\sqrt{2R\delta}$
$\bar{a}^*$	$\sqrt{2R\sigma}$	$\sqrt{2R\delta}$
p^*	$E\sqrt{\sigma/8R}$	$E\sqrt{\delta/8R}$
P^*	$P_{_h}(\sigma)$	$P_{_h}(\delta)$

Thus in this work, δ, σ and μ are chosen to be the three input parameters.

It may often provide better physical insights and is more computationally efficient if a formula is made dimensionless. To achieve this for the GW formulations, two non-dimensionalised forms will be described below. The first one, termed the σ-form, is mainly based on the original version proposed by Greenwood and Tripp [3] where σ is involved as the main scaling factor. The second one, termed the δ-form, is similar but uses δ as the main scaling factor.

These two forms are closely associated with the non-dimensional parameter α introduced in [4] and its reciprocal α' defined as

$$\alpha = \frac{\sigma}{\delta}; \quad \alpha' = \frac{1}{\alpha} = \frac{\delta}{\sigma} \tag{25}$$

These two parameters will appear in the two non-dimensional forms respectively. For an arbitrary physical quantity or function q, its non-dimensionalised version q^* can be determined by a scaling factor λ_q:

$$q = \lambda_q q^* \tag{26}$$

Table 1 lists the scaling factors for those quantities in the two non-dimensional forms. The non-dimensional expressions of the functions $p(r), w(r)$ and P for the two forms in terms of the non-dimensional parameters α (or α') and μ are presented below.

The σ-form:

$$p^*(r^*, \alpha') = \mu \int_{w^*(r^*,\alpha')+r^{*2}}^{\infty} \left[z_s^* - w^*(r^*, \alpha') - r^{*2}\right]^{3/2} \phi(z_s^* - \alpha')\, dz_s^* \tag{27}$$

$$w^*(r^*, \alpha') = \frac{2}{\pi} \int_0^{\bar{a}^*} \frac{t^*}{t^* + r^*} p^*(t^*, \alpha') \mathbf{K}(k) dt^* \tag{28}$$

$$P^*(\alpha', \mu) = \frac{3\sqrt{2}}{8} \int_0^{\bar{a}^*} 2\pi r^* p^*(r^*, \alpha') dr^* \tag{29}$$

The δ-form:

$$p^*(r^*, \alpha) = \frac{\mu}{\alpha} \int_{w^*(r^*,\alpha)+r^{*2}}^{\infty} \left[z_s^* - w^*(r^*, \alpha) - r^{*2}\right]^{3/2} \phi(z_s^* - 1)\, dz_s^* \tag{30}$$

$$w^*(r^*, \alpha) = \frac{2}{\pi} \int_0^{\bar{a}^*} \frac{t^*}{t^* + r^*} p^*(t^*, \alpha) \mathbf{K}(k) dt^* \tag{31}$$

$$P^*(\alpha, \mu) = \frac{3\sqrt{2}}{8} \int_0^{\bar{a}^*} 2\pi r^* p^*(r^*, \alpha) dr^* \tag{32}$$

Note that w^* and P^* have the same expression, whilst only p^* is slightly different in the two forms. Most importantly, the total contact force between two rough spheres can now be written as

$$P(\delta, \sigma, \mu) = P_h(\delta)P^*(\alpha, \mu) = P_h(\sigma)P^*(\alpha', \mu) \tag{33}$$

i.e. the Hertzian load P_h for the smooth contact with the same overlap δ, or with the roughness σ as the equivalent overlap, is acting as the scaling factor for the total force P in each form. Particularly, the overlap δ (or the roughness σ) has now been separated from the other two non-dimensional parameters α (or α') and μ, and therefore the total contact load $P(\delta, \alpha', \mu)$ (or $P(\sigma, \alpha', \mu)$) as a function of the three variables can now be obtained by simply evaluating the non-dimensional load $P^*(\alpha, \mu)$ (or $P^*(\alpha', \mu)$), only involving α (or α') and μ, and then multiplying it by the Hertzian load $P_h(\delta)$ (or $P_h(\sigma)$). The total computational costs therefore can be reduced substantially by an order of magnitude in comparison with the original formulations. In addition, the non-dimensional forms can make the curve fitting of $P(\delta, \alpha, \mu)$ (or $P(\sigma, \alpha', \mu)$) more accurate in the next stage which will be discussed in Section 7.

4 Recovering of the Hertzian solutions for smooth spheres

It is theoretically important that the GW model can reduce to the Hertzian solution for smooth spheres when the roughness $\sigma = 0$. However, this is not apparent. In fact, it is easy to verify that by directly setting $w(r)$ to be the Hertzian deformation $w_h(r)$ in (19) gives rise to a zero pressure distribution $p(r) = 0$, which is obviously incorrect. Equally, numerical difficulties arise when directly applying the condition $\sigma = 0$ to the non-dimensional version (27) or (30) because $\alpha = 0$ or $\alpha' = \infty$.

In what follows, it will be proved that the GW model does recover the Hertzian solution, but as the limit when $\sigma \to 0$ if the parameter μ is assumed to be fixed.

Suppose that when σ is close to zero, both the deformation and pressure distributions of the sphere are also close to the Hertzian solutions for the smooth contact case, and thus can be expressed as

$$w(r) = w_h(r) - \Delta w(r); \quad \text{with } \Delta w(r) \ll w_h(r) \tag{34}$$

and

$$p(r) = p_h(r) - \Delta p(r); \quad \text{with } \Delta p(r) \ll p_h(r) \tag{35}$$

Note that when $\sigma \to 0$, the zero-centred normal probability distribution function $\phi(z_s)$ tends to the Dirac delta function, denoted here as $\Delta(z_s)$, so that (19) becomes

$$p(r) = C\int_{d(r)}^{\infty} \big[z_s - d(r)\big]^{3/2}\Delta(z_s)\, dz_s = C\left[z_0 - w(r) - \frac{r^2}{2R}\right]^{3/2} \tag{36}$$

From (13) it follows

$$p_h(r) - \Delta p(r) = C\big[\Delta w(r)\big]^{3/2} \tag{37}$$

thus

$$p_h(r) \approx C\big[\Delta w(r)\big]^{3/2} \tag{38}$$

or

$$\Delta w(r) \approx \left[\frac{p_h(r)}{C}\right]^{2/3} = \left(\frac{p_0}{C}\right)^{2/3}\left(1 - \frac{r^2}{a^2}\right)^{1/3} \tag{39}$$

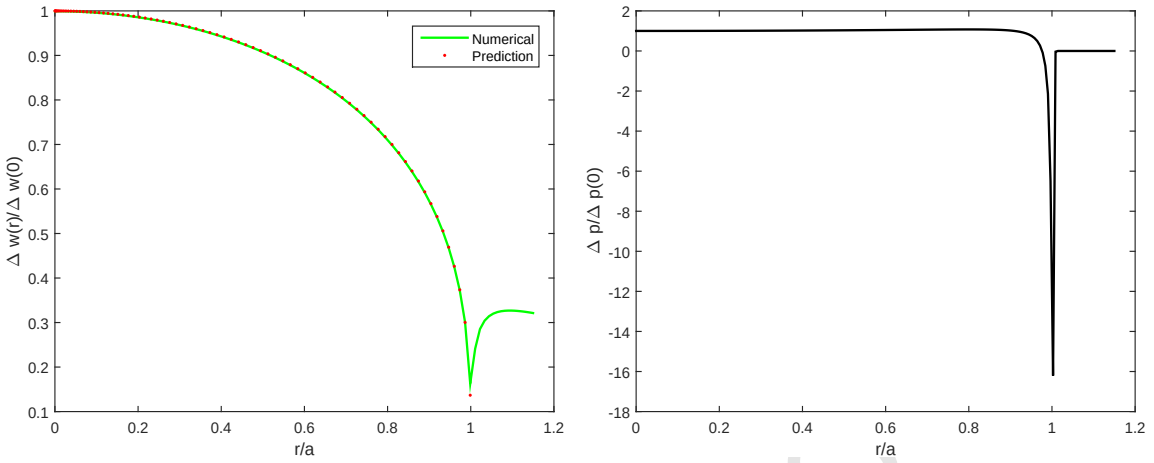

(a) (b)

Figure 4: Numerically simulated distributions of: (a) $\Delta w(r)$; and (b) $\Delta p(r)$

The maximum difference between $\Delta w(r)$ and $w_h(r)$ occurs at $r = 0$. Define the relative deformation difference, ϵ_w, as

$$\epsilon_w = \frac{\Delta w(0)}{w_h(0)} = \frac{(p_0/C)^{2/3}}{w_0} = \left(\frac{16\sqrt{2}}{3\pi\mu}\alpha\right)^{2/3} \tag{40}$$

i.e. ϵ_w is proportional to $\alpha^{2/3}$, and thus converges with α to zero with a speed of 2/3.

For a given overlap δ and a fixed μ, $\alpha = \sigma/\delta \to 0$ as $\sigma \to 0$, thus

$$\lim_{\sigma\to 0} \Delta w(r) = 0$$

The *linear* relationship between $w(r)$ and $p(r)$ in (20) is also applicable to $\Delta w(r)$ and $\Delta p(r)$:

$$\Delta w(r) = \frac{4}{\pi E}\int_0^{\bar{a}} \frac{t}{r+t}\Delta p(r)\mathbf{K}(k)\, dt \tag{41}$$

Although an explicit expression for $\Delta p(r)$ may not be available, the numerical simulation shown below indicates that $\Delta p(r)$ is almost constant except in a very small region at $r = a$. So it may assume that

$$\Delta p(r) \approx \Delta p(0) \tag{42}$$

From (41), it has

$$\Delta p(0) = \frac{E}{2a}\Delta w(0) \tag{43}$$

Then the relative pressure difference, ϵ_p, between $\Delta p(r)$ and $p_h(r)$ at $r = 0$ is

$$\epsilon_p = \frac{\Delta p(0)}{p_h(0)} \approx \frac{E}{2a}\frac{\Delta w(0)}{p_o} = \epsilon_w \tag{44}$$

as $w_0 = 2ap_0/E$.

Hence it is concluded that the GW model converges to the Hertzian model when $\sigma \to 0$:

$$\lim_{\sigma\to 0} w(r) = w_h(r); \quad \lim_{\sigma\to 0} p(r) = p_h(r) \tag{45}$$

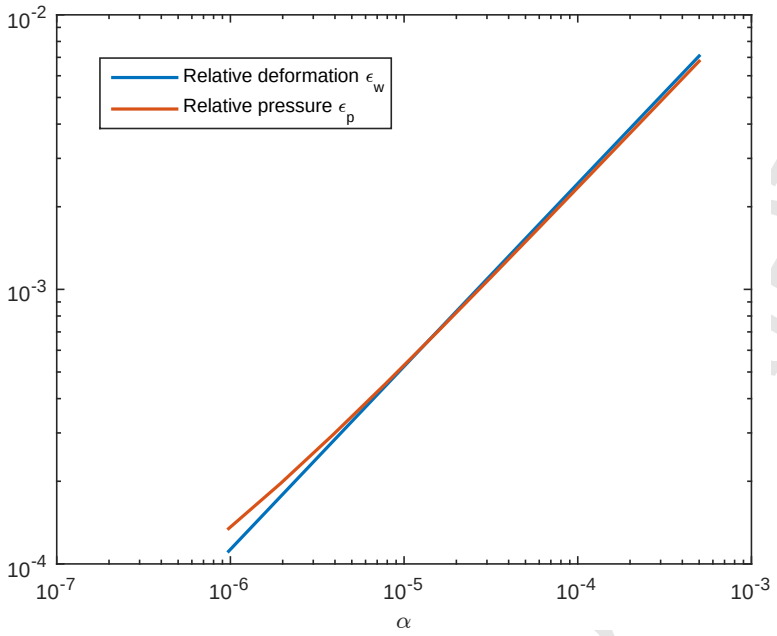

Figure 5: Relative deformation and pressure differences, ϵ_w and ϵ_p, against α

The above theoretical argument is numerically verified by using the computational procedures described in the next section. Figures 4(a) and (b) show the numerically calculated distributions of $\Delta w(r)/w_h(0)$ and $\Delta p(r)/\Delta p(0)$, respectively, for $\alpha = 10^{-4}$ and $\mu = 2$. Figure 4(a) also illustrates the predicted distribution of $\Delta w(r)/w_h(0)$ by (39). An excellent agreement has been observed between the numerical and predicted distributions over the whole contact area $[0, a]$. Figure 4(b) illustrates that $\Delta p(r)$ is almost constant for the whole contact area except in a very small region closed to $r = a$, where the (absolute) value increases sharply. Figure 5 depicts how the relative deformation and pressure differences, ϵ_w and ϵ_p, converge to zero with α. It confirms that $\epsilon_w \approx \epsilon_p$ and that the convergent speed is indeed 2/3.

5 Numerical Solutions and Computational Issues

Due to the inter-dependence between the pressure $p(r)$ and the deformation $w(r)$, and the non-integrable part involving the Gaussian distribution, as shown in Equations (17) and (20), an explicit expression between the overlap δ and the contact force P cannot be established. Thus, numerical solutions must be sought to obtain the force P for a given set of values for δ, σ (or α) and μ. In what follows, the original formulations of the GW model are used for discussion, but the proposed procedure and relevant numerical techniques are equally applicable to the two non-dimensional forms introduced in Section 3.

5.1 Numerical solutions of the pressure and deformation distributions and the contact force

Because Equations (17) and (20) are coupled to implicitly define the pressure distribution $p(r)$ in terms of the deformation of the sphere $w(r)$ over the contact area, both equations need to be solved simultaneously to obtain a numerical solution. Although this can be fulfilled in a different manner, the Newton-Raphson method will be employed in this work due to its quadratic convergence.

Note that the contact radius $\bar{a}$ may not be known *in prior* because the contact radius for rough surface contact may not be determined precisely. Although a sufficiently large value of $\bar{a}$ can be estimated based on the given overlap δ and the roughness σ, an appropriate value should be used to achieve a high numerical accuracy when the contact region is discretised as described below.

Firstly, the interval of the contact area $[0,\ \bar{a}]$ is discretised into m discrete points $\mathbf{r}_m = [r_1, \cdots, r_m]^T$. In this work these points are taken to be the integration points (or abscissae) of the chosen numerical integration quadrature for the integral in Equation (20) which will be discussed later, and the corresponding weights are assumed to be $\mathbf{s}_m = [s_1, \cdots, s_m]^T$. Then Equation (17) can be discretized as

$$p_i = C \int_{d_i}^{\infty} (z_s - d_i)^{3/2} \phi(z_s)\, dz_s \equiv C g(w_i) \tag{46}$$

where

$$g(w_i) = \int_{d_i}^{\infty} (z_s - d_i)^{3/2} \phi(z_s) dz_s;\ d_i = w_i - \delta + r_i^2/(2R)$$

and Equation (20) becomes

$$w_i = \frac{4}{\pi E} \sum_{j=1}^{m} s_j \alpha_{ij} p_j \tag{47}$$

where the coefficients α_{ij} are

$$\alpha_{ij} = \frac{r_j}{r_i + r_j} \mathbf{K}(k_{ij}); \quad k_{ij} = \frac{2\sqrt{r_i r_j}}{r_i + r_j} \tag{48}$$

Thus the equation to be satisfied at discrete point i is governed by

$$F_i(p_1, \cdots, p_m) = p_i - C g(w_i) = 0 \tag{49}$$

Since this equation has to be satisfied at all the discrete points, $r_i\,(i = 1, \cdots, m)$, it leads to a nonlinear system of equations in vector format

$$\mathbf{F}(\mathbf{p}) = \mathbf{p} - C\mathbf{g}(\mathbf{w}) = 0 \tag{50}$$

where the four vectors involved are

$$\mathbf{F} = [F_1, \cdots, F_m]^T; \mathbf{p} = [p_1, \cdots, p_m]^T; \mathbf{w} = [w_1, \cdots, p_m]^T; \mathbf{g}(\mathbf{w}) = [g(w_1), \cdots, g(w_m)]^T$$

To solve the above nonlinear system of equations in terms of $\mathbf{p}$ by the Newton-Raphson method, the function $\mathbf{F}$ is expanded by the Taylor series in the neighbourhood of $\mathbf{p}$ with an infinitesimal increment $\delta\mathbf{p}$

$$\mathbf{F}(\mathbf{p} + \delta\mathbf{P}) = \mathbf{F}(\mathbf{p}) + \mathbf{J}\delta\mathbf{p} + \mathrm{O}(\delta\mathbf{p}^2) \tag{51}$$

where $\mathbf{J}$ is the Jacobian matrix of the vector function $\mathbf{F}$

$$\mathbf{J} = \nabla\mathbf{F};\ \text{or}\ J_{ij} = \frac{\partial F_i}{\partial p_j} \tag{52}$$

By ignoring the 2nd and higher order terms in (51), the increment $\delta\mathbf{p}$ can be obtained by

$$\delta\mathbf{p} = -\mathbf{J}^{-1}\mathbf{F}(\mathbf{p}) \tag{53}$$

The final solution $\mathbf{p}$ is achieved when the iterative process converges starting from a trial solution that can be chosen to be the Hertzian pressure distribution. Then the total contact force can be obtained by numerically integrating the converged discrete pressure distribution $\mathbf{p}$ over the entire contact area

$$P(\delta) = 2\pi \sum_{j=1}^{m} s_j r_j p_j \tag{54}$$

5.2 Computational issues

There are several computational issues involved in the above numerical procedure that may have some significant impact on the overall computational efficiency and accuracy so thus need to be discussed in detail.

5.2.1 Numerical integrations

Three integrals involved in Equations (17) $\sim$ (20) need to be evaluated numerically. Although many numerical integration quadratures can be used, such as the trapezium or Simpson rule with equally spaced integration points, the Gaussian quadrature is adopted in the current work due to its high algebraic accuracy. As the two integrals in Equations (17) and (20) have the same integral domain which is the contact area $[0, \bar{a}]$, the same Gaussian points and weights are used. Note that this is also the requirement of the Newton-Raphson solution procedure outlined in the previous subsection.

The integral in (21) has a different integral domain and thus should be evaluated using a different number of Gaussian points. Although the upper bound of the domain should be infinity in theory, a limited value based on the given roughness σ can be adopted instead.

5.2.2 Evaluation of the Jacobian matrix

The Jacobian $\mathbf{J}$ needs to be evaluated at each Newton-Raphson iteration. However, it is difficult to obtain the analytical expression. In this work, a finite difference approximation to $\mathbf{J}$ is employed. Let $\mathbf{J}_j$ be the j-th column of $\mathbf{J}$, and $\mathbf{e}_j = [0, \cdots, 1, \cdots, 0]^T$ be a unit vector with only the j-component being unity. Then $\mathbf{J}_j$ is approximated by

$$\mathbf{J}_j = \frac{1}{\epsilon_j}\Big[\mathbf{F}(\mathbf{p} + \epsilon_j\, \mathbf{e}_j) - \mathbf{F}(\mathbf{p})\Big], \qquad j = 1, ..., m \tag{55}$$

where

$$\epsilon_j = \epsilon \max\{p_j, \epsilon\}$$

in which ϵ is a *perturbation* parameter. Note that ϵ should be neither too large to sacrifice the quadratic convergence of the Newton-Raphson method, nor too small to cause numerical instability. The numerical test, to be presented in the next section, shows that $\epsilon = 10^{-6}$ is sufficient to maintain the quadratic convergence without causing any numerical instability.

5.2.3 Determination of coefficients α_{ij}

The coefficients α_{ij} defined in (48) play a crucial role in the current numerical solution procedure. An efficient approach to determine their values are described below. Introducing a ratio $\lambda_{ij} = r_i/r_j, \alpha_{ij}$ can now be expressed in a slightly different form

$$\alpha_{ij} = \frac{1}{1+\lambda_{ij}}\mathbf{K}(k_{ij}); \quad k_{ij} = \frac{2\sqrt{\lambda_{ij}}}{1+\lambda_{ij}} \tag{56}$$

As λ_{ij} is non-dimensional and fixed for a given m of the integration quadrature regardless of the contact radius $\bar{a}$, α_{ij} are also non-dimensional and fixed. Note that $k_{ij} = k_{ji}$, thus $\mathbf{K}(k_{ij}) = \mathbf{K}(k_{ji})$. Since it is computationally intensive to obtain the value of the elliptic function $\mathbf{K}(k)$, utilising the symmetry of k_{ij} can halve the computational costs in evaluating

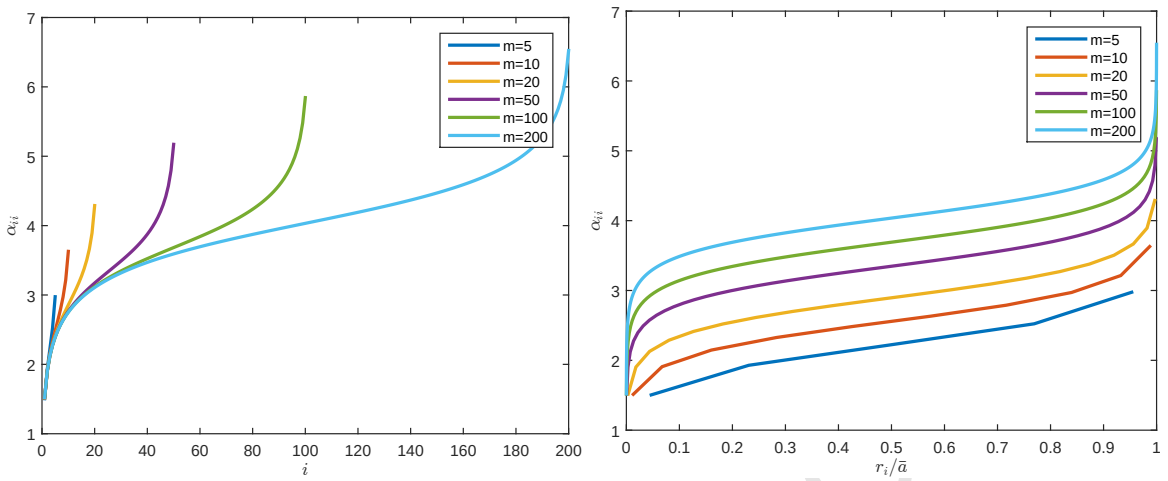

(a) (b)

Figure 6: Distribution of diagonal coefficients α_{ii}

α_{ij}. Note that a relatively effective way to compute $\mathbf{K}(k)$ is by the arithmetic-geometric mean described in [27].

However, a singularity problem occurs when evaluating the diagonal terms α_{ii} since $\lambda_{ii} = k_{ii} = 1$, while $\mathbf{K}(1)$ is infinity. This singularity is avoided in [3] by introducing an auxiliary function $\mathcal{L}(\xi)$, but its inverse has to be found numerically in order to evaluate $w(r)$. In [20] or [24], the problem is avoided by assuming that the pressure is constant over each discretised element or element, and therefore the integral (20) over the element can be explicitly expressed, but at the expense of a reduced solution accuracy. In this work, the singularity problem is resolved based on the fact that the Hertzian pressure and deformation distributions are the analytical solutions to (20): for an arbitrarily given Hertzian pressure distribution

$$\bar{p}_h(r) = \bar{p}_0(1 - r^2/\bar{a}^2)^{1/2}$$

over the contact region $[0, \bar{a}]$, the deformation from (20) is given by the Hertzian solution

$$\bar{w}_h(r) = \bar{w}_0(1 - r^2/2\bar{a}^2)$$

where $\bar{w}_0 = \pi\bar{p}_0\bar{a}/2E$. Thus it is natural to require that α_{ii} be determined in such a manner so that for the given Hertzian pressure distribution $\bar{p}_h(r)$, the calculated w_i from (47) should be equal to $\bar{w}_h(r_i)$:

$$\bar{w}_h(r_i) = \frac{4}{\pi E}\sum_{j=1}^{m} s_j\alpha_{ij}\bar{p}_h(r_j) \tag{57}$$

which leads to

$$\alpha_{ii} = \frac{1}{s_i\bar{p}_h(r_i)}\left[\frac{\pi E}{4}\bar{w}_h(r_i) - \sum_{j=1,j\neq i}^{m} s_j\alpha_{ij}\bar{p}_h(r_j)\right] \tag{58}$$

It can be verified that $\alpha_{ii}(i = 1, ..., m)$ are independent of the contact radius $\bar{a}$ and the material property E as expected. The distribution of α_{ii} in terms of i or the (scaled) position $x_i/\bar{a}$ in the contact region $[0, \bar{a}]$ against the number of integration points m in the Gaussian quadrature is illustrated in Figure 6, indicating that the lower terms converge when m increases.

In summary, all the coefficients α_{ij} are solely determined by the number of integration points m (and their positions) for any chosen integration quadrature and thus can be pre-calculated

Table 2: The pressure errors in the Newton-Raphson iterations for different α ($\mu = 4$)

Iteration	$\alpha = 0.01$	$\alpha = 0.1$	$\alpha = 1.0$
1	7.26e-2	1.77e-1	2.36e-1
2	3.81e-2	5.00e-2	1.27e-2
3	7.53e-3	4.38e-3	8.28e-5
4	4.68e-4	2.81e-5	2.11e-11
5	1.80e-6	8.58e-10	1.14e-17
6	2.42e-11	2.77e-16	
7	1.40e-15		

when m is given and used for any overlap and surface roughness. This feature, together with the property $\mathbf{K}(k_{ij}) = \mathbf{K}(k_{ji})$, significantly increases the computational efficiency of the preceding numerical solution procedure. The specific approach to determining the diagonal terms α_{ii} not only eliminates the singularity problem, but also maintains a high numerical accuracy of the integration quadrature.

6 Numerical Results and Validation

This section presents and validates some numerical results obtained following the numerical procedures proposed in the previous sections to ensure that the computed contact forces $P(\delta, \sigma, \mu)$ are sufficiently accurate to be curve-fitted in the next section. The validation of some results will be conducted against the known results presented in the literature. There are several parameters involved in the numerical procedure proposed in the preceding section that need to be selected appropriately to ensure a high solution accuracy and overall computational efficiency. Selections of their values will also be discussed.

6.1 Convergence of the Newton-Raphson procedure

The Newton-Raphson method should exhibit a quadratic convergence when properly implemented. This property may be affected if the chosen value of the perturbation parameter ϵ in (55) is too large. The residual error at iteration i is defined as

$$\epsilon_i = ||\delta \mathbf{p}_i||/\|\mathbf{p}_i\| \tag{59}$$

where $\delta \mathbf{p}_i$ is the pressure increment at the iteration and $\mathbf{p}_i$ is the updated pressure after the iteration. The Hertzian pressure distribution $p_{_h}(r)$ is taken as the initial guess for $p(r)$. The perturbation parameter ϵ is set to be 10^{-6}. For a fixed $\mu = 4$ and $m = 100$, the history of the residual errors during the iterations for different α is recorded in Table 2. It is clear that a quadratic convergence is achieved for all the α values, indicating that $\epsilon = 10^{-6}$ is an appropriate value. It is also evident that faster convergent speeds are achieved for larger α, and the typical number of iterations needed to reach an accuracy of around 10^{-6} is about 4 or 5.

Table 3: The computed $P^*(\alpha, \mu)$ for different numbers of Gaussian points m ($\mu = 4$)

m	$\alpha = 0.1$	$\alpha = 1$	$\alpha = 5$
5	**0.970**1255	**2.0143**635	**11.077**996
10	**0.9770**791	**2.0139**965	**11.0706**76
20	**0.97696**59	**2.01388**68	**11.07166**0
50	**0.976951**6	**2.013870**9	**11.071798**
100	**0.9769507**	**2.0138699**	**11.071806**
200	**0.9769506**	**2.0138697**	**11.071807**

6.2 Selections of numerical parameters

The following parameters need to be specified in the numerical procedure: 1) the contact radius $\bar{a}$; 2) the number of Gaussian integration points m used in the evaluation of the integrals (20) and (21); and 3) the number of Gaussian integration points and the upper bound of the integral domain for the integral (17).

The pressure distribution $p(r)$ reduces when r increases and further drops to a very small or zero value. As the contact radius $\bar{a}$ is unknown *in prior*, it should be specified sufficiently large so that the actual contact region is fully covered, but not too large to cause a large portion of the (nearly) zero-pressure region because the integration or discretisation points located in the region will be wasted. The follow formula to determine $\bar{a}$ appears to work well:

$$\bar{a} = (1.75 + \min\{\alpha, |\alpha'|\})a \tag{60}$$

where a is the contact radius of a smooth contact case with the same overlap δ (for $0 < \alpha < 1$) or the equivalent overlap σ (for $\alpha' = 1/\alpha < 1$).

The number of Gaussian integration points for the integral (17) is chosen to be 10. The upper bound is taken to be 5σ, as this will statistically cover 99.99994% of possible peak heights, and thus should not affect the final solution accuracy.

The number of Gaussian points m has a major influence on the computational costs and the accuracy of the computed total force P, or $P^*(\alpha, \mu)$. In order to select a proper value, the following accuracy convergence test has been conducted: different numbers of m are used to compute $P^*(\alpha, \mu)$ for a number of combinations of α and μ values. The results are presented in Table 3, in which the significant digits of the computed force for each m are highlighted which is obtained by comparing the force value with the one for the next m. It appears that $m = 20$ is required to obtain an accuracy of about 10^{-5}, but it is remarkable that even $m = 5$ can achieve an accuracy of 10^{-3}. Nevertheless, to ensure that all the results are sufficiently accurate, m is taken to be 200 in all the subsequent computations.

6.3 Comparisons of pressure distributions and effective contact radii

Some selected numerical results obtained in this work are validated by comparing them against those presented by Johnson in [4], including: 1) the maximum contact pressure $p(0)$ normalised by the maximum Hertzian pressure p_0 for different α and μ; and 2) the effective contact radius a^* normalised by the Hertzian contact radius a as a function of α and μ. The maximum Hertzian pressure p_0 and contact radius a are obtained from smooth sphere contact under the same contact load P. The effective contact radius a^* is arbitrarily defined

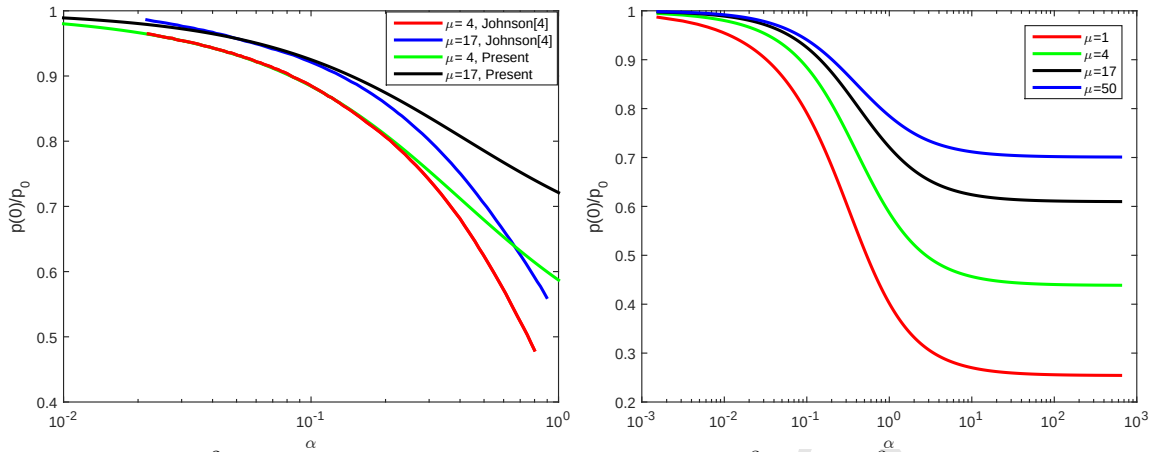

(a) $10^{-2} \leq \alpha \leq 1$; $\mu = 4, 17$ (b) $10^{-3} \leq \alpha < 10^{3}$; $\mu = 1, 4, 17, 50$

Figure 7: The ratio of the maximum contact pressure $p(0)$ to the maximum Hertzian pressure p_0 against α and μ: (a) comparison of the present work with Johnson's [4] for $\alpha < 1$ and two μ; (b) the present work for wider ranges of α and μ

by Greenwood and Tripp [3] as

$$a^* = \frac{3\pi \int_0^{\bar{a}} rp(r)dr}{4 \int_0^{\bar{a}} p(r)dr} \tag{61}$$

Figure 7(a) depicts a comparison of the ratio $p(0)/p_0$ for $10^{-3} < \alpha \leq 1$ and two values of $\mu = 4$ and 17 between the present work and those presented in Figure 13.12 on page 420 in [4]. It shows an excellent agreement in the range $0.02 < \alpha < 0.2$ for the curve $\mu = 4$, and in a narrower range $0.045 < \alpha < 0.065$ for the curve $\mu = 17$. However, the difference between the present work and the referenced work [4] becomes noticeable and increases when α increases towards $\alpha = 1$ for $\mu = 4$ and 17, and when α decreases from 0.045 for $\mu = 17$. No comparison, however, can be made for $\alpha > 1$ as no corresponding results are available in the referenced work.

Nevertheless, in order to shed a further insight into the contact behaviour of rough surfaces, the maximum effective pressure $p(0)$ over the Hertzian pressure p_0 from the current work is provided in Figure 7(b) for a much wider range of α ($10^{-3} < \alpha < 10^3$) and a larger set of $\mu(= 1, 4, 17$ and $50)$. The figure shows that the ratio $p(0)/p_0$ increases towards 1 when α decreases to zero regardless of μ, as proved in Section 4; while α decreases with the increase of α but asymptotically reaches a *non-zero* limit value that monotonically increases with μ. On the contrary, it may be reasonably deduced from the two curves in the referenced work that when α increases the ratio decreases towards zero in an accelerated manner.

Figure 8(a) shows a comparison of the ratio a^*/a for $10^{-3} < \alpha \leq 1$ and two values of $\mu = 4$ and 17 between the present work and those presented in Figure 13.13 on page 421 in [4]. Again, it shows a very good agreement in the range $0.02 < \alpha < 0.2$ for the curve $\mu = 4$, and in a narrower range $0.06 < \alpha < 0.1$ for the curve $\mu = 17$. However, the difference between the present work and the referenced work becomes larger when α increases towards $\alpha = 1$ for $\mu = 4$ and 17, and when α decreases from 0.06 for $\mu = 17$. Again, no comparison can be made for $\alpha > 1$ as no corresponding results are available in the referenced work.

Similar to the ratio $p(0)/p_0$, the effective contact radius a^* over the Hertzian contact radius a from the current work is provided in Figure 8(b) for a much wider range of α ($10^{-3} < \alpha < 10^3$) and a larger set of $\mu(= 1, 4, 17$ and $50)$. The figure shows a very similar behaviour as in the ratio $p(0)/p_0$ that the ratio a^*/a increases towards 1 when α decreases to zero regardless of

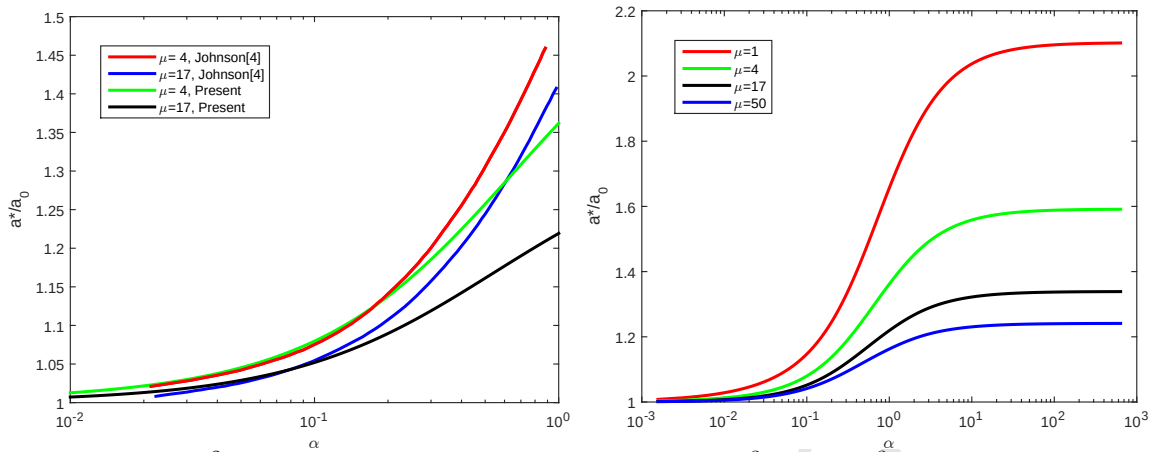

(a) $10^{-2} \leq \alpha \leq 1$; $\mu = 4, 17$ (b) $10^{-3} \leq \alpha < 10^{3}$; $\mu = 1, 4, 17, 50$

Figure 8: The ratio of the effective contact radius a^* to the Hertzian contact radius a_0 against α and μ: (a) comparison of the present work with Johnson's [4] for $\alpha < 1$ and two μ; (b) the present work for wider ranges of α and μ

μ, as expected; while the ratio increases with the increase of α but asymptotically reaches a limit value that monotonically increases with μ. On the contrary, it may also be deduced from the two curves in the referenced work that when α increases the ratio increases in an accelerated manner.

In summary, because both maximum pressure $p(0)$ and effective contact radius a^* in the present work agree very well with those in the referenced work for certain ranges of α and μ, it is with high confidence that the current implementation of the GW model is correct, while the observed discrepancies might be due to some unknown reasons in the referenced work. It may also be concluded that the effect of the parameter μ for large α may not be secondary as claimed in [4].

6.4 Effects of input parameters on pressure distributions

Effects of the two parameters α and μ on the pressure distribution $p(r)$ over the entire contact area $[0, \bar{a}]$ and the effective contact radius a^* have been extensively discussed, for instance, in [2, 4] and elsewhere, so thus will not be discussed in detail here.

Figure 9 illustrates the effective pressure distributions for three different $\alpha = 0.1, 1$ and 10 and four different $\mu = 1, 4, 10$ and 17, where the Hertzian distribution is for the smooth contact under the same contact load P, and the vertical line of each curve indicates the position of the corresponding effective radius a^*. As expected, the increase of α reduces the maximum pressure $p(0)$ but spreads the load over a greater contact area $\bar{a}$ and thereby leading to a larger effective contact radius a^*.

7 A Normal Contact Interaction Law for Rough Spheres in DEM

A contact interaction law in the DEM defines an explicit relationship between the contact force, the overlap and other contact characteristics of the two contacting particles. Most commonly used interaction laws in the DEM are explicit and simple functions of the overlap

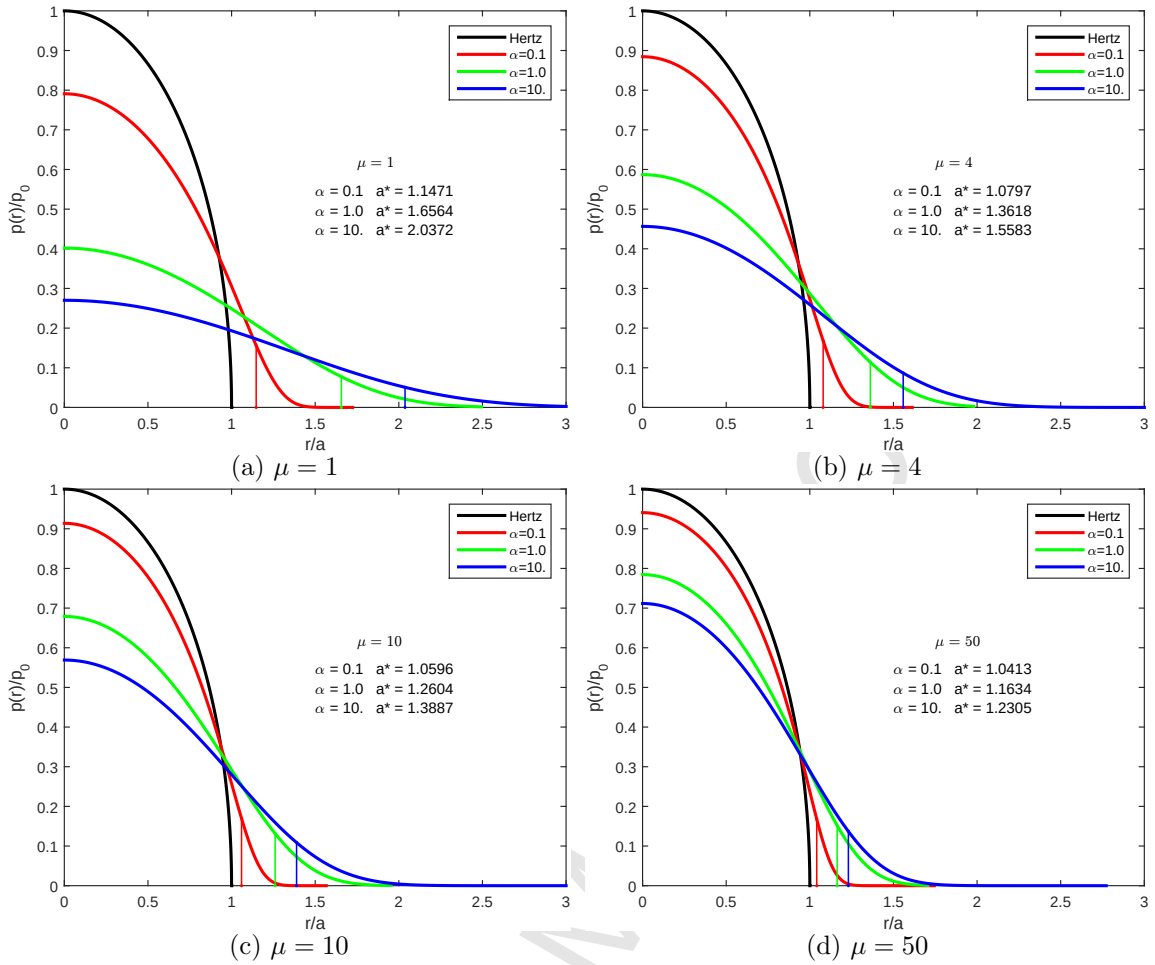

(a) $\mu = 1$ (b) $\mu = 4$

(c) $\mu = 10$ (d) $\mu = 50$

Figure 9: Effective pressure distributions for different α and μ (the vertical line of each curve indicates the position of effective radius a^*)

and other contact features, if present. However, the GW model defines, via Equations (17), (20) and (21), a very complicated but most importantly implicit relationship between the total contact force P, the overlap δ, and the roughness parameters σ and μ, and therefore cannot be directly employed in the DEM. In order to obtain a normal interaction law that can be readily used in the DEM, an explicit expression for $P(\delta, \sigma, \mu)$ needs to be established, mainly through curve-fitting procedures, from the numerical solutions that build the bridge between the GW model and the interaction law in the DEM.

7.1 Explicit expressions of non-dimensional contact loads

Following the discussion in Section 4, the total contact force $P(\delta, \sigma, \mu)$ can be expressed in the two equivalent non-dimensional forms, the $\sigma-$ and $\delta-$ versions, as

$$P(\delta, \sigma, \mu) = P_h(\delta)P^*(\alpha, \mu) = P_h(\sigma)P^*(\alpha', \mu) \tag{62}$$

Hence, in principle, an explicit expression for P will be fully determined if the non-dimensional load, either $P^*(\alpha, \mu)$ or $P^*(\alpha', \mu)$, can be explicitly defined.

Referring to Figure 10, any straight line from the origin on the $\delta - \sigma$ plane has a constant slope of α (or $1/\alpha'$) for a given μ, hence the non-dimensional load P^* along the line is the

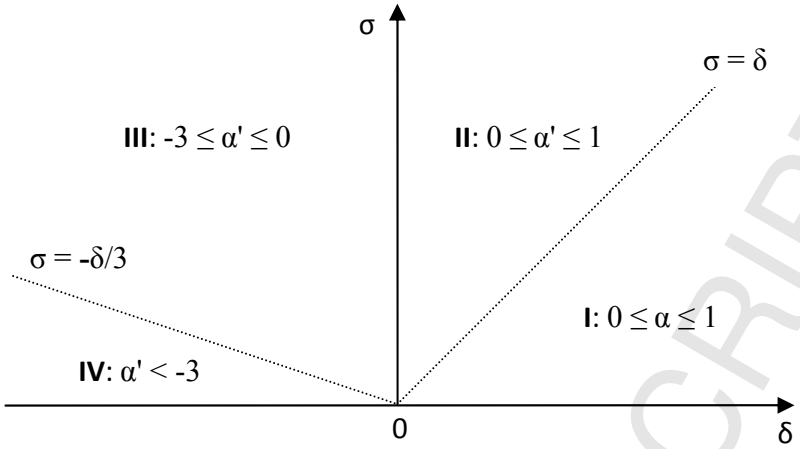

Figure 10: The division of the $\delta - \sigma$ plane into four cases

same. However, because σ is non-negative, while δ can be positive (in overlap) or negative (in separation), the range of α or α' is infinity: $-\infty < \alpha, \alpha' < \infty$. Also the meaning of $P_h(\delta)$ is less clear for the δ version of the non-dimensional form when δ is negative. Therefore, using either non-dimensional form alone may encounter some inconvenience or even numerical difficulties. A more effective approach is to combine the both forms to express the total force P for different cases. To this end, the (upper half) $\delta - \sigma$ plane is divided into two parts: 1) $\sigma < \delta$, or $0 < \alpha \leq 1$; and 2) $\sigma > \delta$, i.e. $-\infty < \alpha' \leq 1$, and to use $P^*(\alpha, \mu)$ for the first part and $P^*(\alpha', \mu)$ for the second. Also note that

$$\lim_{\alpha' \to -\infty} P^*(\alpha', \mu) = 0 \tag{63}$$

Thus from a practical point of view, the lower bound of α' can be taken as -3 since $P^*(-3, \mu)$

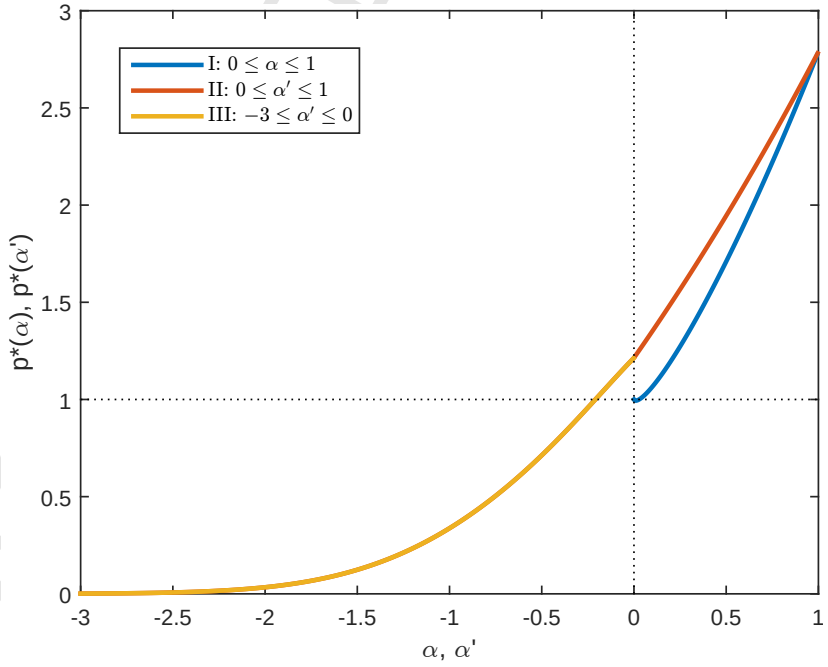

Figure 11: The non-dimensional load curve vs $0 \leq \alpha \leq 1$ and $-3 \leq \alpha' \leq 1$ for $\mu = 10$

is already sufficiently small ($\sim 10^{-3}$), and $P^*(\alpha', \mu)$ can be set to zero beyond

$$P^*(\alpha', \mu) = 0, \quad \alpha' < -3 \tag{64}$$

As also shown in Figure 11 which is the combination of both $P^*(\alpha, \mu)$ and $P^*(\alpha', \mu)$ curves for a fixed $\mu = 10$, $P^*(\alpha', \mu)$ behaves differently in $0 < \alpha' < 1$ from in $-3 < \alpha' < 0$, and hence should be treated separately in the context of curve-fitting. As a result, the $\delta - \sigma$ plane is now divided into four cases, I to IV, as shown in Figure 10, and three explicit approximations to P^*, denoted as $P_1^*(\alpha, \mu)$, $P_2^*(\alpha', \mu)$ and $P_3^*(\alpha', \mu)$ for the first three cases, are sought.

Compared with the parameter α (or α'), the parameter μ plays a less primary and clear role. A two-step curve-fitting approach will be adopted to obtain the empirical expressions. In the first step, a limited number of values for μ are selected, and for each fixed μ, a curve-fitting for $P^*(\alpha, \mu)$ or $P^*(\alpha', \mu)$ will be conducted. In the second step, the coefficients of the empirical functions attained will be further curve-fitted in terms of μ or tabulated as discrete values to be represented later in the DEM by interpolating functions such as cubic splines.

Following [4], μ is assumed to be in the range of $[1, 50]$, and seven values of $\mu = 1, 2, 4, 10, 20, 35$ and 50 are selected. For each μ, 200 equally spaced values of α in [0, 1] and 1000 of α' in $[-3, 1]$ are used to generate both curves $P^*(\alpha, \mu)$ and $P^*(\alpha', \mu)$ using the numerical procedure outlined in Section 5. The computed entire non-dimensional load curve for $\mu = 10$ is depicted in Figure 11.

In deriving the three approximations $P_i^*(i = 1, 2, 3)$ for a fixed μ, the continuity of the whole load P^* requires that

$$P_1^*(1, \mu) = P_2^*(1, \mu); \quad P_2^*(0, \mu) = P_3^*(0, \mu) \tag{65}$$

Thus for each case, the empirical expression is obtained not purely by best-fitting but by a constrained curve-fitting in order to meet the above continuity conditions, and any additional conditions. The empirical formulas for the three cases will be derived in the following subsections.

7.2 Empirical formula for Case I

The curves of $P^*(\alpha, \mu), 0 \leq \alpha \leq 1$, for the seven values of μ are depicted in Figure 12(a). The curve-fitted formula $P_1^*(\alpha, \mu)$ is chosen to be a cubic polynomial of α for each μ

$$P_1^*(\alpha, \mu) = b_0(\mu) + b_1(\mu)\alpha + b_2(\mu)\alpha^2 + b_3(\mu)\alpha^3 \tag{66}$$

subject to two conditions:

$$P_1^*(1, \mu) = P^*(1, \mu); \quad P_1^*(0, \mu) = P^*(0, \mu) = 1 \tag{67}$$

where the first condition is the continuity requirement of (65); while the added second condition is the direct consequence that the GW model reduces to the Hertzian model for smooth surfaces (see Section 4) when $\sigma = \alpha = 0$:

$$P^*(0, \mu) = 1 \tag{68}$$

which immediately leads to the conclusion that

$$b_0(\mu) = 1 \tag{69}$$

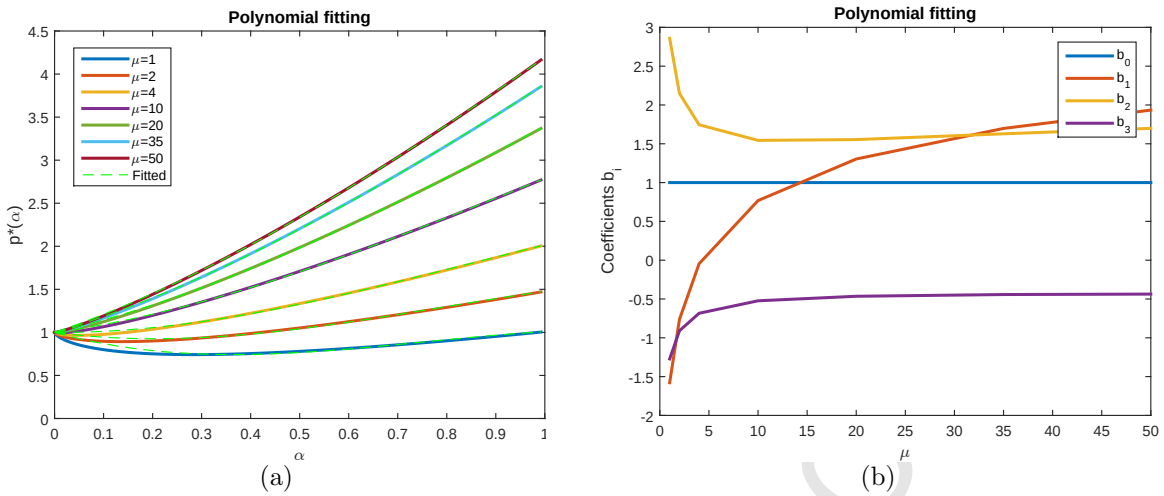

Figure 12: Case I - $0 \leq \alpha \leq 1$: (a) Computed $P^*(\alpha, \mu)$ and cubic polynomial fitted curves; (b) The coefficients of the cubic polynomial

Table 4: Case I ($0 \leq \alpha \leq 1$): Coefficients of the cubic polynomial for different μ

coef.	μ						
	1	2	4	10	20	35	50
b_0	1.0	1.0	1.0	1.0	1.0	1.0	1.0
b_1	-1.5786	-0.7621	-0.0452	0.7680	1.3038	1.6977	1.9339
b_2	2.8588	2.1478	1.7448	1.5438	1.5539	1.6284	1.6988
b_3	-1.2721	-0.9086	-0.6837	-0.5233	-0.4649	-0.4426	-0.4368
	Fitted formula						
b_0	1.0						
b_1	$1.55\ln(\mu) - 1.60\mu^{0.2442}$						
b_2	$1.52/\mu + 0.00655\mu + 1.35$						
b_3	$-0.055\ln(\mu) - 1.15\mu^{-0.619} - 0.12$						

Before using curve-fitting to determine the remaining coefficients $b_i (i = 1, 2, 3)$, it must be pointed out that the contact force P for rough surfaces should be larger than the Hertzian load P_h under the same overlap δ, i.e. $P^*(\alpha, \mu) > 1$. It is, however, not the case as demonstrated in Figure 12(a) since for all μ, and when α is close to 0, $P^*(\alpha, \mu) < 1$. This is a defect of the current GW model, but the issue will not be fully addressed in the current work. To partially mitigate this problem, $P_1^*(\alpha, \mu)$ is set to satisfy two additional conditions

$$P_1^*(1/3, \mu) = P^*(1/3, \mu); \quad P_1^*(2/3, \mu) = P^*(2/3, \mu) \tag{70}$$

Thus $P_1^*(\alpha, \mu)$ is now the interpolation function passing through four points of the curve $P^*(\alpha, \mu)$ at $\alpha = 0, 1/3, 2/3$ and 1.

The fitted curves using $P_1^*(\alpha, \mu)$ for the seven values of μ are plotted in Figure 12(a). It is evident that a very good fitting has been achieved except when α is close to 0, but this is intended.

The four coefficients $b_i (i = 0, \cdots, 3)$ of $P_1^*(\alpha, \mu)$ for the seven values of μ are displaced in Figure 12(b) and listed in Table 4. It is clear that all four coefficients converge when μ increases. An alternative (best-)fitted formula obtained by applying a nonlinear least-squares procedure for each coefficient is also presented in the table.

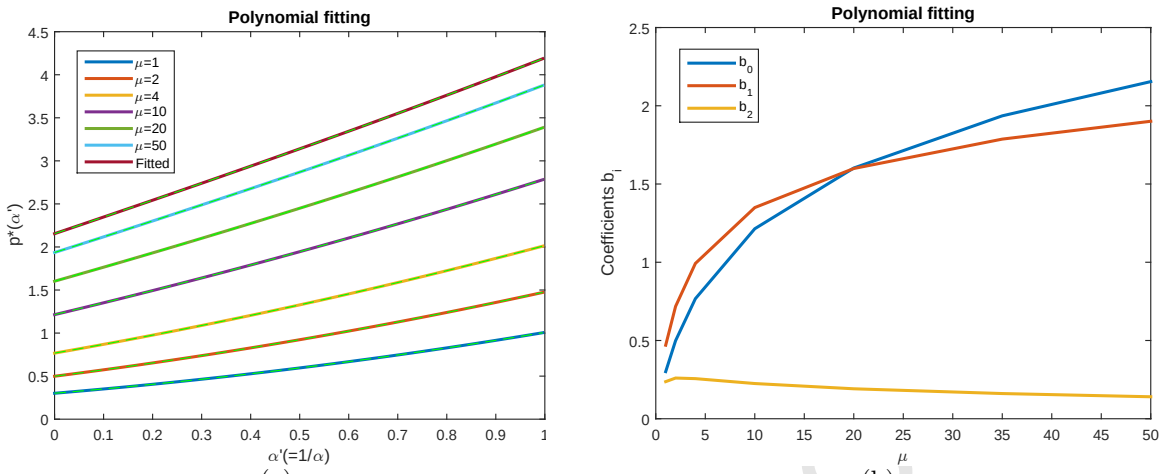

Figure 13: Case II - $0 \leq \alpha' \leq 1$: (a) Computed $P^*(\alpha', \mu)$ and quadratic fitted curves; (b) The coefficients of the quadratic polynomial

Table 5: Case II ($0 \leq \alpha' \leq 1$): Coefficients of the quadratic polynomial for different μ

coef.	μ						
	1	2	4	10	20	35	50
b_0	0.3011	0.4989	0.7672	1.2141	1.6022	1.9357	2.1544
b_1	0.4700	0.7181	0.9924	1.3494	1.5991	1.7869	1.9010
b_2	0.2370	0.2601	0.2563	0.2250	0.1914	0.1610	0.1404
	Fitted formula						
b_0	$-0.398\ln(\mu) + 5.965\mu^{0.1163} - 5.677$						
b_1	$0.371\ln(\mu) + 0.478\mu^{-0.0015}$						
b_2	$0.004858\exp(0.0514\mu) - 0.0035\mu + 0.2526$						

7.3 Empirical formula for Case II

Similar to the previous case, the curves of $P^*(\alpha', \mu), 0 \leq \alpha' \leq 1$ for the seven values of μ are depicted in Figure 13(a). The formula $P_2^*(\alpha, \mu)$ is chosen to be a quadratic of α for each μ

$$P_2^*(\alpha, \mu) = b_0(\mu) + b_1(\mu)\alpha + b_2(\mu)\alpha^2 \tag{71}$$

subject to two continuity conditions

$$P_2^*(0, \mu) = P^*(0, \mu); \quad P_2^*(1, \mu) = P^*(1, \mu) \tag{72}$$

By adding an additional condition

$$P_2^*(1/2, \mu) = P^*(1/2, \mu)$$

$P_2^*(\alpha, \mu)$ can be determined as the interpolation function passing through the three points of $P^*(\alpha', \mu)$ at $\alpha' = 0, 1/2$ and 1.

The fitted curves using $P_2^*(\alpha, \mu)$ for the seven values of μ are plotted in Figure 13(a). It is evident that a very good fitting has been achieved. The three coefficients $b_i (i = 0, 1, 2)$ of $P_2^*(\alpha, \mu)$ for the seven values of μ are displaced in Figure 13(b) and listed in Table 5. It appears that b_2 converges when μ increases. An alternative (best-)fitted formula for each coefficient is also presented in the table.

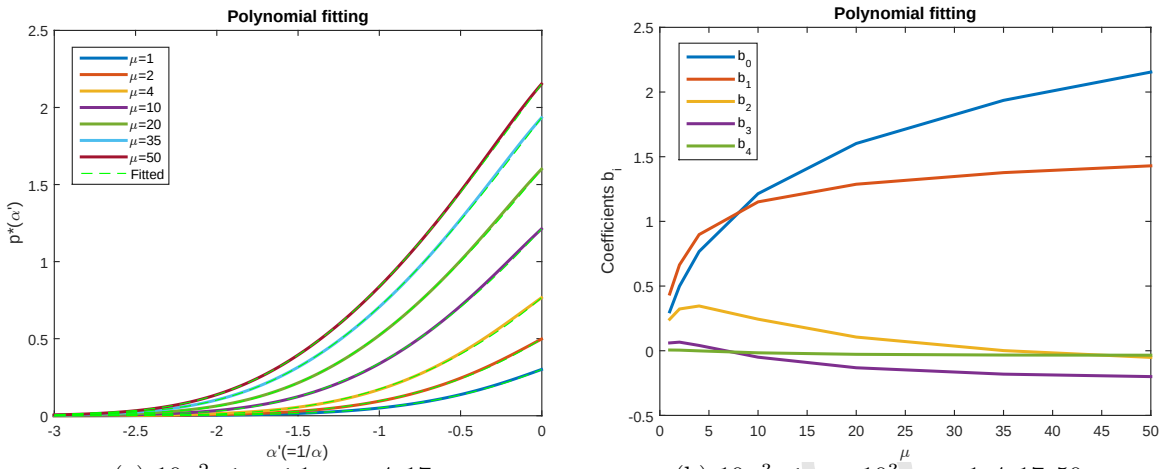

(a) $10^{-2} \le \alpha \le 1$; $\mu = 4, 17$ (b) $10^{-3} \le \alpha < 10^3$; $\mu = 1, 4, 17, 50$

Figure 14: (a) Computed $P^*(\alpha, \mu)$ and quartic polynomial fitted curves; (b) The coefficients of the quartic polynomial

Table 6: Case III ($-3 \le \alpha' \le 0$): The coefficients of the quartic polynomial for different μ

coef.	μ						
	1	2	4	10	20	35	50
b_0	0.3011	0.4989	0.7672	1.2141	1.6022	1.9357	2.1544
b_1	0.4385	0.6638	0.8981	1.1507	1.2872	1.3770	1.4295
b_2	0.2431	0.3227	0.3460	0.2440	0.1058	0.0012	-0.0516
b_3	0.0604	0.0665	0.0408	-0.0498	-0.1316	-0.1810	-0.1999
b_4	0.0057	0.0047	-0.0010	-0.0161	-0.0277	-0.0333	-0.0345
	Fitted formula						
b_0	$0.2284\ln(\mu) + 0.2769\mu^{0.3913}$						
b_1	$0.4998\ln(\mu) - 0.5067\mu^{0.2724} + 0.9405$						
b_2	$-0.8103\exp(-0.6351\mu) - 9.211\mu^{0.01958} + 9.881$						
b_3	$0.5035\exp(-0.03976\mu) + 0.0029\mu - 0.4124$						
b_4	$0.05555\exp(-0.06902\mu) + 0.0001782\mu - 0.04497$						

7.4 Empirical formula for Case III

The curves of $P^*(\alpha', \mu), -3 \le \alpha' \le 1$ for the seven values of μ are depicted in Figure 14(a). The curve-fitted formula $P_1^*(\alpha, \mu)$ is chosen by trial to be a quartic polynomial of α for each μ

$$P_3^*(\alpha, \mu) = b_0(\mu) + b_1(\mu)\alpha + b_2(\mu)\alpha^2 + b_3(\mu)\alpha^3 + b_4(\mu)\alpha^4 \tag{73}$$

subject to two conditions

$$P_3^*(-3, \mu) = P^*(-3, \mu); \quad P_3^*(0, \mu) = P^*(0, \mu) \tag{74}$$

By adding an additional condition

$$P_2^*(1/2, \mu) = P^*(1/2, \mu)$$

$P_2^*(\alpha, \mu)$ can be determined as the interpolation function passing through the five points of $P^*(\alpha', \mu)$ at $\alpha' = -3, -9/4, -6/4, -3/4$ and 0.

The fitted curves using $P_3^*(\alpha,\mu)$ for the seven values of μ are plotted in Figure 14(a). Again a very good fitting has been achieved. The five coefficients $b_i(i=0,\cdots,4)$ of $P_3^*(\alpha,\mu)$ for the seven values of μ are displaced in Figure 14(b) and are also listed in Table 6. An alternative (best-)fitted formula for each coefficient is also presented in the table.

In summary, the final explicit form of the curve-fitted normal contact interaction law for rough spheres can be expressed as

$$P(\delta,\sigma,\mu)=\begin{cases} P_h(\delta)P_1^*(\alpha,\mu); & \delta\geq\sigma \\ P_h(\sigma)P_2^*(\alpha',\mu); & 0<\delta<\sigma \\ P_h(\sigma)P_3^*(\alpha',\mu); & -3\sigma<\delta<0 \\ 0; & \delta<-3\sigma \end{cases} \tag{75}$$

where $P_i^*(i=1,2,3)$ are polynomials of α or α' with degree of up to 4 and their coefficients, in either discrete or fitted form, are presented in Tables 4, 5 and 6 respectively. However, because of the nature of curve-fitting procedures, all the formulas are valid for $\mu\in[1,50]$ and should be used with caution for μ outside the range.

8 An Illustrative Example

To demonstrate the effect of surface roughness on some properties of particle assemblies, the normal contact law for spheres with surface roughness developed in the preceding sections is implemented in a DEM code, and the following illustrative example is modelled.

The example considers the effects of surface roughness on the random dense packing of a particle assembly with different sized spheres in a rigid cylindrical container under two packing conditions: 1) the act of the gravity; 2) the act of a vertical uni-axial compression but with no gravity.

The radii (in cm) of six different sized spheres in the assembly are respectively: 0.275(22%), 0.3275(24%), 0.3775(22%), 0.4125(9%), 0.4625(21%), and 0.5450(2%), where the numbers in the brackets are the corresponding percentages of spheres in the system. The total number of particles is 10,189. The material properties of the particles are: Young's modulus E= 2.1GPa, Poisson's ratio $\nu=0.3$, and density $\rho=2800kg/m^3$. The cylindrical container has an inner radius of $R=6.2cm$ and all the inner surfaces are smooth.

The packing starts from an initial packing configuration, as shown in Figure 15(a), which is generated by the algorithm described in [28]. The initial packing density is about 0.495 and the height of the packing is around $H=31.75cm$. The radii of the spheres are temporally enlarged by 1% during the initial packing generation but are set back to their actual values after the generation procedure is completed. This is to ensure that all the particles in the initial packing will (almost) not be in contact with one another for the levels of surface roughness considered in the subsequent modelling, so that the effects of surface roughness on the packing behaviour of the system can be fairly assessed.

The surface roughness σ of a particle is set to be proportional to its radius r: $\sigma=\sigma_r\ r$, where the roughness ratio σ_r is assumed to be the same for all the particles in the assembly. Four levels of surface roughness ratios $\sigma_r=[0.0,0.001,0.005,0.01]$ are considered for the two packing simulation cases, where $\sigma_r=0.0$ corresponds to a smooth surface case.

Both the sphere-sphere contact and the sphere-surface contact are modelled using the normal interaction law obtained in the last section, with the second roughness parameter μ taken to be 10. It is well known that the coefficient of friction between two contacting surfaces is

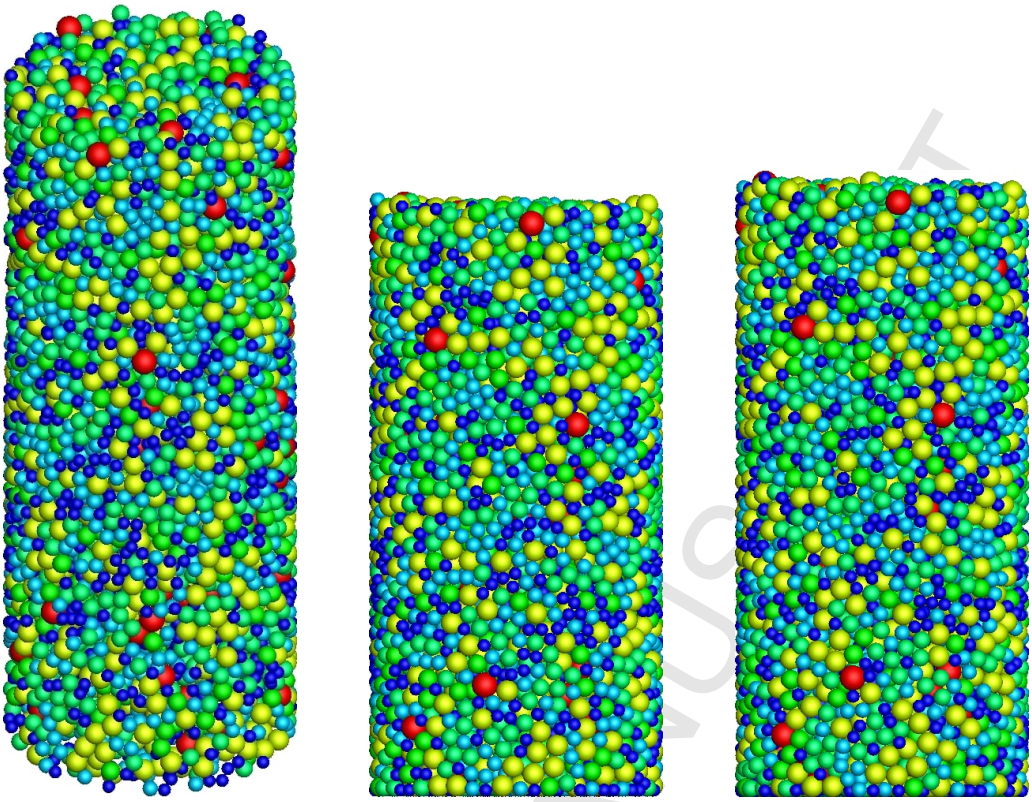

(a) Initial packing configuration

(b) Final packing ($\sigma_r = 0$)

(c) Final packing ($\sigma_r = 0.01$)

Figure 15: Initial packing Configuration (a); and Final packing Configurations for $\sigma_r = 0$ (b) and $\sigma_r = 0.01$ (b). Six different sized particles are used. Colors denote particle sizes

largely dictated by their surface roughness. However, since there is a lack of a qualitative relationship between surface roughness and a coefficient of friction, no friction is considered either between the spheres or between the spheres and the cylinder.

In the first particle packing simulation, the particles are allowed to settle to an equilibrium packing configuration under the action of the gravity and with the presence of a viscous damping. The two final packing configurations corresponding to $\sigma_r = 0.0$ and 0.01 are displayed in Figure 15(a) and (b) respectively, where a visually small height difference between the two packings indicates that surface roughness makes the packing slightly looser, as expected.

The final packing density and the density distribution in height are numerically compared for the four roughness levels. Figure 15(a) depicts the effect of the roughness ratio on the overall packing density, showing an almost linearly decreasing packing density with the increase of the roughness ratio. An exactly 2% density reduction from the smooth surface case is observed for $\sigma_r = 0.01$. Figure 15(b) further reveals how the surface roughness affects the density distribution along the height. The distribution is obtained by dividing the assembly into 5000 equal-spaced layers in the height and then accurately calculating the particle volume fraction in each layer. Clearly, the surface roughness makes the packing looser along the whole height, but the effect becomes more notable at higher heights, as expected again. This can be fully explained by the interaction law presented in Figure 11.

In the second packing simulation, a smooth flat surface with a const vertical velocity of -0.05cm/s is applied to the top of the initial packing to compress the assembly up to a com-

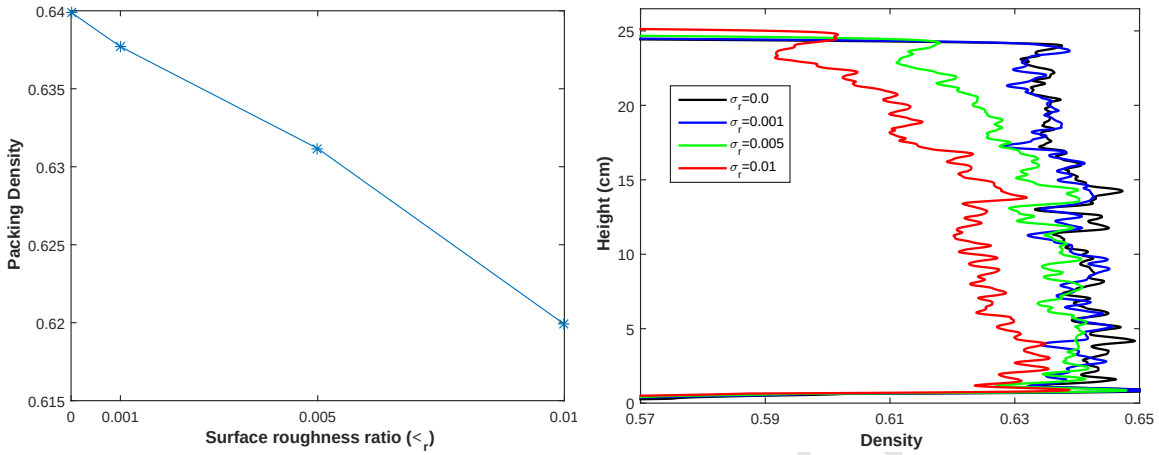

(a) Overall packing density (b) Density distribution in height

Figure 16: Overall packing density (a) and the packing density distributions in height (b) for four different surface roughness ratios $\sigma_r = 0.0, 0.001, 0.005, 0.01$

pression distance of 7cm, or equivalent to achieving the final packing density of 0.635. Define the compression strain as $\epsilon_c = d/H$ where d is the compression distance of the top surface, and the compression stress as $\sigma_c = F/\pi R^2$ where F is the the total reaction force acting on the top surface. The compression strain-stress curves for the four roughness ratios, shown in Figure 17(a), illustrate that larger compression forces are required for larger roughness ratios, as expected. The compression stresses at two specific compression strain values $\epsilon_c = 0.2$ and 0.2175 are also plotted in Figure 17(b) for the four roughness ratios, and a nearly linear relationship between the roughness ratio and the compression stress is observed for both strain levels. These two strain values are chosen because the first strain $\epsilon = 0.2$ corresponds to the point that the stress for the smooth surface case is about to steadily increase from (nearly) zero, while the second $\epsilon_c = 0.2175$ is the maximum compression strain applied.

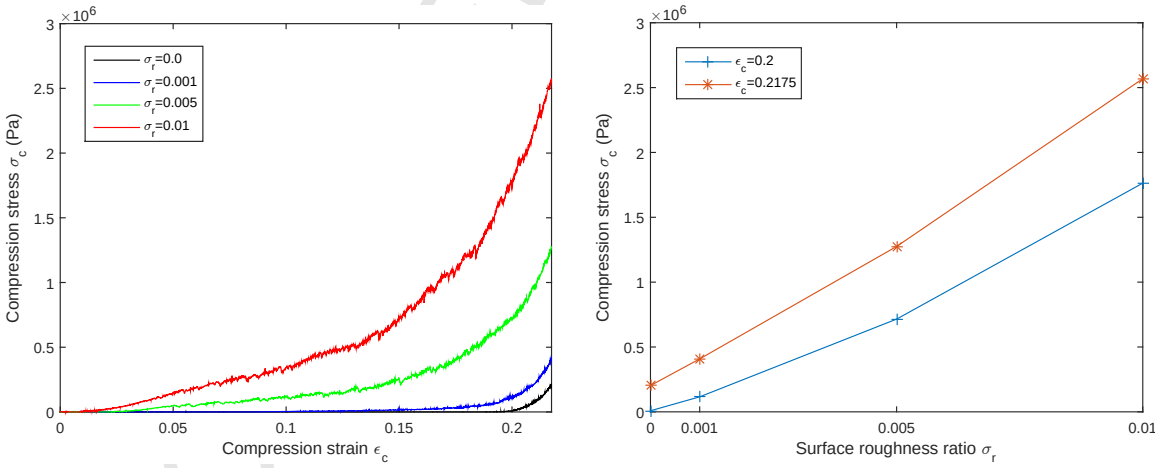

(a) $\epsilon_c - \sigma_c$ curves (b) σ_c at two ϵ_c values

Figure 17: The compression strain-stress curves (a) and the compression stresses at two compression strain levels $\epsilon_c = 0.2, 0.2175$ (b) for four surface roughness ratios $\sigma_r = 0.0, 0.001, 0.005, 0.01$

9 Concluding Remarks

This work has developed a new normal contact law for spheres with surface roughness based on the classic GW model. Due to the inter-dependence between the contact pressure p_r and the deformation $w(r)$ in the model, and the non-integrable part involving the Gaussian distribution, an explicit expression for the contact force P, in terms of the overlap δ and the surface roughness parameters σ and μ, has to be obtained through numerical solutions. A Newton-Raphson based iterative solution procedure has been proposed to effectively and accurately obtain the contact pressure and deformation distributions and the total force.

The essential components of this numerical procedure include the use of the Gaussian quadrature to evaluate three integrals, the adoption of a finite-difference approximate to the Jacobian matrix, and the determination of the coefficients α_{ij} and particularly the diagonal terms α_{ii}. It reveals that the coefficients α_{ij} are solely determined by the number of integration points m used for the chosen integration quadrature and thus can be pre-calculated. These features not only significantly increase the computational efficiency of the proposed numerical solution procedure, but also maintain the high accuracy of the numerical solutions.

On the basis of the numerical results obtained and validated against some existing results in the literature, an explicit predictive formula for calculating the normal contact force between two rough spheres has been derived through curve-fitting techniques. Owing to the explicit nature, this new normal contact law can be readily incorporated into the existing discrete element modelling procedure, thus making the first step towards the development of stochastic discrete element modelling framework. The illustrative example presented in Section 8 has already demonstrated some possible effects of surface roughness on particle systems.

However, it is noted that since all the contact quantities, $p(r)$, $w(r)$ and P, are random fields and variables, what are currently obtained are their expected values. To obtain an interaction law of a random nature, other statistic properties, such as the variance of the contact force as a function of δ, σ and μ, need to be derived. Also as mentioned in Section 6, the current GW model gives a lower than expected total contact force, indicating that there may be some fundamental issues to be addressed. When these issues are resolved, a stochastic interaction law for spheres with surface roughness can be established. Then its effectiveness and applicability to many engineering applications can be fully assessed.

References

[1] P. A. Cundall, O. D. L. Strack. A discrete numerical model for granular assemblies. *Gotechnique.* 29(1):47-65, 1979.

[2] J. A. Greenwood, J. B. Williamson. Contact of nominally flat surfaces. *Proceedings of the Royal Society of London A: Mathematical, Physical and Engineering Sciences.* 295(1442):300-319, 1966.

[3] J. A. Greenwood, J. H. Tripp. The elastic contact of rough spheres. *Journal of Applied Mechanics.* 34(1):153-159, 1967.

[4] K. L. Johnson. *Contact Mechanics.* Cambridge University Press, 1985.

[5] D. R. Owen, Y. T. Feng, E. de Souza Neto, F. Wang, M. G. Cottrel, F. A. Pires, J. Yu. The modelling of Multi-fracturing Solids and Particulate Media. *International Journal for Numerical Methods in Engineering.* 60(1): 317-340, 2004.

[6] R. P. Jensen, P. J. Bosscher, M. E. Plesha, T. B. Edil. DEM simulation of granular mediastructure interface: effects of surface roughness and particle shape. *International Journal for Numerical and Analytical Methods in Geomechanics*. 23(6):531-547, 1999.

[7] L. Wang, J. Y. Park, Y. Fu. Representation of real particles for DEM simulation using X-ray tomography. *Construction and Building Materials*. 21(2):338-346, 2007.

[8] M. Lu, G. R. McDowell. The importance of modelling ballast particle shape in the discrete element method. *Granular Matter*. 9(1-2):69-80, 2007.

[9] J. F. Ferellec, G. R. McDowell. A simple method to create complex particle shapes for DEM. *Geomechanics and Geoengineering: An International Journal*. 3(3):211-216, 2008.

[10] X. Garcia, J. P. Latham, J. Xiang, J. P. Harrison. A clustered overlapping sphere algorithm to represent real particles in discrete element modelling. *Geotechnique*. 59(9):779-84, 2009.

[11] W. Zhou, G. Ma, X. L. Chang, Y. Duan. Discrete modeling of rockfill materials considering the irregular shaped particles and their crushability. *Engineering Computations*, 32(4):1104-1120, 2015.

[12] M. M. Shamsi, A. A. Mirghasemi. Numerical simulation of 3D semi-real-shaped granular particle assembly. *Powder Technology*. 221:431-46, 2012.

[13] J. R. Barber, M. Ciavarella. Contact mechanics. *International Journal of Solids and Structures*. 37(1):29-43, 2000.

[14] J. F. Archard. Elastic deformation and the laws of friction. *In Proceedings of the Royal Society of London A: Mathematical, Physical and Engineering Sciences*. 243(1233): 190-205, 1957.

[15] A. Majumdar, B. Bhushan. Role of fractal geometry in roughness characterization and contact mechanics of surfaces. *ASME Journal of Tribology*. 112(2):205-216, 1990.

[16] H. M. Stanley, T. Kato. An FFT-based method for rough surface contact. *Journal of Tribology*. 119(3):481-485, 1997.

[17] W. R. Chang, I. Etsion, D. B. Bogy. An elastic-plastic model for the contact of rough surfaces. *Journal of Tribology*. 109(2):257-263, 1987.

[18] Y. Zhao, D. M. Maietta, L. Chang. An asperity microcontact model incorporating the transition from elastic deformation to fully plastic flow. *Journal of Tribology*. 122(1):86-93, 2000.

[19] R. L. Jackson, I. Green. A finite element study of elasto-plastic hemispherical contact against a rigid flat. *Journal of Tribology*. 127(2):343-354, 2005.

[20] A. Beheshti, M. M. Khonsari. Asperity micro-contact models as applied to the deformation of rough line contact. *Tribology International*. 52:61-74, 2012.

[21] D. Cohen, Y. Kligerman, I. Etsion. The effect of surface roughness on static friction and junction growth of an elastic-plastic spherical contact. *Journal of Tribology*. 131(2):021404, 2009.

[22] E. R. Gelinck, D. J. Schipper. Deformation of rough line contacts. *Journal of Tribology*. 121(3):449-454, 1999.

[23] L. Li, I. Etsion, F. E. Talke. Elasticplastic spherical contact modeling including roughness effects. *Tribology Letters*. 40(3):357-363, 2010.

[24] A. Beheshti, M. M. Khonsari. On the Contact of Curved Rough Surfaces: Contact Behavior and Predictive Formulas. *Journal of Applied Mechanics*. 81(11):111004, 2014.

[25] J. Kato. *Numerical Modelling for Stochastic Discrete Elements*. Maters Thesis, Civil and Computational Engineering Centre, Swansea Univeristy, UK, 2006.

[26] Y. T. Feng, T. Zhao, J. Kato, W. Zhou. Stochastic Discrete Element Modelling of Rough Particles A Random Normal Interaction Law. *Chinese Journal of Computational Mechanics*. 33(4):629-636, 2016.

[27] M. Abramowitz, I. A. Stegun. *Handbook of Mathematical Functions* Dover Publications, Chapter 17.6, 1965.

[28] K. Han, Y. T. Feng, D. R. J. Owen. Sphere Packing With a Geometric Based Compression Algorithm. *Powder Technology*, 155(1):33-41, 2005.

Highlights:

- **This is believed to be a first attempt towards establishing a stochastic discrete element modelling framework by considering particle surface roughness.**

- **A normal contact interaction law based on the classic Greenwood and Williamson (GW) model for spheres with rough surfaces is developed.**

- **Two non-dimensional forms of the model that have a substantial impact on the computational efficiency are discussed.**

- **A Newton-Raphson based iterative solution procedure is proposed to effectively and accurately obtain the contact force in terms of the overlap and two surface roughness parameters. The related key components of the procedure are addressed in detail.**

- **The numerical results obtained are validated and then curve-fitted to derive an empirical formula as a new normal interaction law for spheres with surface roughness.**